



Highly crumpled graphene nano-networks as electrocatalytic counter electrode in photovoltaics

Jae-Yup Kim^{a,1}, Jang Yeol Lee^{a,1}, Keun-Young Shin^{a,1}, Hansol Jeong^{a,b}, Hae Jung Son^{a,b}, Chul-Ho Lee^c, Jong Hyuk Park^a, Sang-Soo Lee^{a,c}, Jeong Gon Son^{a,**}, Min Jae Ko^{a,b,c,*}

^a Photo-Electronic Hybrids Research Center, Korea Institute of Science and Technology (KIST), Seoul, 02792, Republic of Korea

^b Green School, Korea University, Seoul, 02841, Republic of Korea

^c KU-KIST Graduate School of Converging Science and Technology, Korea University, Seoul, 02841, Republic of Korea

ARTICLE INFO

Article history:

Received 25 January 2016

Received in revised form 2 April 2016

Accepted 5 April 2016

Available online 7 April 2016

Keywords:

Crumpled graphene

Electrocatalytic activity

Dye-sensitized solar cell

Counter electrode

ABSTRACT

Highly crumpled graphene-based three dimensional (3D) interconnected and hierarchically porous conducting networks were prepared for application as electrocatalytic counter electrode (CE) in dye-sensitized solar cells (DSSCs). Finely and hierarchically crumpled graphene was synthesized from Fe₂O₃/graphene oxide (GO) hybrids via a one-step chemical etching–reduction process with HI solution. The synthesized crumpled graphene exhibited not only 24 times higher specific surface area, but also superior dispersibility in aqueous solution compared to conventional reduced graphene oxide (rGO). Owing to its superior solution processability and comparable electrical conductivity, the crumpled graphene could be assembled into 3D interconnected films on the substrates simply by drop casting, without any binders. In addition, although the crumpled graphene was not modified by dopants or high-temperature annealing, it showed much higher electrocatalytic activity for the I[−]/I₃[−] redox couple compared to that of rGO, which is mainly attributed to its significantly larger accessible surface area for electrochemical reduction. As a result, the DSSC containing the crumpled graphene CE exhibited 2.8 times enhanced conversion efficiency ($\eta = 5.15\%$) compared to that containing a rGO electrode ($\eta = 1.86\%$).

© 2016 Elsevier B.V. All rights reserved.

1. Introduction

Graphene, a one-atom-thick planar sheet consisting of sp²-bonded carbon atoms packed in a honeycomb lattice, has recently attracted much attention for its application in energy conversion and storage devices owing to unique properties including excellent electrical conductivity, high theoretical surface area, and good solution processability [1–11]. In particular, it has been intensively studied as electrocatalytic counter electrode (CE) material for next-generation photovoltaic devices, such as dye-sensitized solar cells (DSSCs) and quantum dot-sensitized solar cells (QDSCs), for replacing the conventional Pt CE [9–18]. Among next-generation photovoltaics, DSSCs have emerged as promising energy sources owing to their low production cost, relatively high conversion efficiency, ease of fabrication, and possible flexibility [18–31]. The

CE in a DSSC plays a critical role in that it catalyzes the reduction of the redox couple in the electrolyte. Although Pt is known to be one of the best electrocatalysts for the conventionally used iodide/triiodide redox couple (I[−]/I₃[−]) in DSSCs, its high cost, rarity, and instability against corrosion stand in the way of its practical use [22,32–35]. On the other hand, carbon-based materials, including graphene, have potential as efficient, low-cost, and chemically stable electrocatalytic materials for DSSC CEs [9–17,31,33].

A vast amount of research has been carried out to develop efficient graphene-based CEs for DSSCs [9–17]. It is important to obtain a high enough electrical conductivity for efficient charge transfer and high electrocatalytic activity for redox couples [11,12]. To meet these requirements, in most cases heteroatoms, such as O, N, or P, were incorporated into the graphitic frameworks as dopants [10,11,14–16,36,37]. In addition, graphene films were generally treated with high-temperature annealing (at 300–600 °C) after deposition, which is not compatible with flexible plastic substrates [9,11,12,14]. Furthermore, in order to deposit graphene films on substrates, such as fluorine-doped tin oxide (FTO) glasses, the graphene is usually mixed with polymer binders and complicated processes, such as electrophoretic deposition, electro-spray coating, or layer-by-layer assembly, are required [10–16].

* Corresponding author at: Photo-Electronic Hybrids Research Center, Korea Institute of Science and Technology (KIST), Seoul, 02792, Republic of Korea.

** Corresponding author.

E-mail addresses: jgson@kist.re.kr (J.G. Son), mjko@kist.re.kr (M.J. Ko).

¹ These authors contributed equally to this work.

Therefore, at present, the development of graphene-based CE *via* simple and facile methods without dopants or high-temperature annealing processes is highly challenging.

With this in mind, we have developed efficient CEs for DSSCs based on highly crumpled graphene, without any dopants or high-temperature annealing processes. Three-dimensional (3D) crumpled graphene with many folds and wrinkles was prepared by a simultaneous chemical etching and reduction process using Fe_2O_3 microcubes as hard templates. The developed crumpled graphene exhibited not only a greatly enhanced specific surface area, but also superior dispersibility in aqueous solution compared to its conventional counterpart (*i.e.*, stacked reduced graphene oxide, rGO). Owing to their superior solution processability, the crumpled graphene particles could be assembled into 3D interconnected macroporous films on FTO glass substrates simply by drop casting, without any binders. Although the crumpled graphene was not modified by dopants or high-temperature annealing, it resulted in a much higher conversion efficiency of the DSSC compared to rGO, mainly due to its significantly enhanced accessible surface area for electrochemical reduction. The preparation process for crumpled graphene and its enhanced dispersibility in aqueous solution were characterized. In addition, the electrochemical activities of the crumpled graphene, rGO, and Pt CEs for the I^-/I_3^- redox couple were systematically compared.

2. Experimental

2.1. Preparation of Fe_2O_3 particles and GO suspension

Polycrystalline $\alpha\text{-Fe}_2\text{O}_3$ particles were prepared by a sol-gel process according to previously reported procedures [7,38]. In brief, 5.4 N NaOH aqueous solution was added to an aqueous solution of 2.0 N $\text{FeCl}_3 \cdot 6\text{H}_2\text{O}$ with vigorous stirring, followed by further stirring at 50 °C for 10 min. The produced ferric hydroxide gel was aged at 100 °C for 8 days in a muffle furnace. The resulting reddish-brown precipitate was washed with deionized (DI) water several times to remove remaining ions, followed by drying and redispersion in DI water. The GO nanosheet suspension was prepared from natural graphite (Bay Carbon, SP-1 graphite) by a modified Hummers' method [39].

2.2. Preparation of $\text{Fe}_2\text{O}_3/\text{GO}$ hybrids

The GO nanosheets were coated on the surface of $\alpha\text{-Fe}_2\text{O}_3$ particles using electrostatic interactions. In order to produce positively charged surface characteristics, a 1 wt% aqueous dispersion of $\alpha\text{-Fe}_2\text{O}_3$ particles was mixed with an excess of 1 wt% polyethyleneimine (PEI, average $M_w = 25$ K, branched, Aldrich) suspension with vigorous stirring overnight at room temperature [40]. Then, the positively charged $\alpha\text{-Fe}_2\text{O}_3$ particles were washed and redispersed in DI water several times to remove unadsorbed PEI. It was confirmed by zeta-potential measurements (Zetasizer, 3000HSA, Malvern Instruments) that the PEI-treated $\alpha\text{-Fe}_2\text{O}_3$ particles and GO nanosheets exhibited positive and negative surface charge, respectively, in the aqueous suspension at neutral pH. In order to coat the GO nanosheets on the surface of the $\alpha\text{-Fe}_2\text{O}_3$ particles, 0.01 wt% GO suspension was added to the 1 wt% PEI-treated $\alpha\text{-Fe}_2\text{O}_3$ suspension with mild stirring for several hours. The obtained particles were purified by sedimentation and redispersion in DI water several times to remove any remaining GO nanosheets.

2.3. Preparation of crumpled graphene counter electrode

Crumpled graphene particles were prepared from $\text{Fe}_2\text{O}_3/\text{GO}$ precursor particles *via* a one-step etching–reduction process using HI solution (57 wt% in water, distilled, 99.95%, Aldrich). The 10 wt%

aqueous HI solution was mixed dropwise under vigorous stirring with a 2.5 wt% aqueous suspension of $\text{Fe}_2\text{O}_3/\text{GO}$ precursor particles. The volume ratio of the HI solution and $\text{Fe}_2\text{O}_3/\text{GO}$ suspension was 1:10. The HI treatment was performed at 90 °C for 24 h, followed by vacuum filtration and washing with DI water. For comparison, stacked rGO was also prepared from the pristine GO suspension without the template *via* the same HI treatment procedure. The 0.1 wt% crumpled graphene (or stacked rGO) aqueous solution was dropped onto FTO glass substrates (Pilkington, TEC-8, 8 Ω/sq), followed by drying at room temperature for several hours. The deposited crumpled graphene films were pressed under 0.5 MPa for 1 min using a press machine, to enhance the adhesion with FTO glass substrates. The thickness of the coated graphene layers was measured using an Alpha-Step IQ surface profiler (KLA Tencor). Pt counter electrodes were also prepared by a thermal decomposition method. A drop of 7 mM H_2PtCl_6 in isopropanol was spread onto an FTO glass substrate (Pilkington, TEC-8, 8 Ω/sq), followed by annealing at 400 °C for 20 min in air.

2.4. Electrode assembly

TiO_2 working electrodes were prepared as described in a previous paper [41]. Briefly, nanocrystalline TiO_2 particles of 20 nm diameter were synthesized by a hydrothermal method, followed by mixing with ethyl cellulose (Aldrich), lauric acid (Fluka), and α -terpineol (Fluka) to give a transparent paste. The weight ratio of the final compositions of the transparent paste was as follows: TiO_2 :ethyl cellulose:lauric acid: α -terpineol = 0.18:0.05:0.02:0.75. In addition, a scattering paste was prepared using TiO_2 particles with 500 nm diameter (G2, Showa Denko, Japan). The prepared pastes were deposited on FTO glass substrates by using the doctor blade technique. Before deposition, a dense TiO_2 blocking layer was coated on the FTO glasses by spin casting of 7.5 wt% Ti(IV) bis(ethyl acetoacetato)-diisopropoxide solution in 1-butanol, followed by annealing at 500 °C for 10 min in air. Then, the transparent paste was deposited onto the pretreated FTO glasses. After drying the deposited transparent paste on a hot plate at 130 °C, the scattering paste was subsequently deposited, followed by annealing at 500 °C for 30 min in air. The annealed TiO_2 electrodes were dipped into a 0.5 mM N-719 dye (Everlight) solution in ethanol for 12 h at room temperature. The dye-adsorbed TiO_2 electrodes were assembled with the CEs using hot melt Surlyn 1702 (Dupont, 60 μm -thick), followed by injection of the electrolyte into the assembled cells through pre-drilled holes on the counter electrodes. The electrolyte was composed of 0.7 M 1-propyl-3-methylimidazolium iodide (PMII, synthesized), 0.03 M I_2 (Aldrich, 99.8%), 0.05 M guanidinium thiocyanate (Aldrich, 97%), and 0.50 M 4-*tert*butylpyridine (TBP) in acetonitrile. The active area for each cell was approximately 0.30 cm^2 , which was confirmed by an image analysis program equipped with a CCD camera (Moticam 1000). Symmetric dummy cells of each counter electrode were also assembled to obtain the impedance spectra and Tafel polarization curves. These dummy cells were fabricated by assembling two identical CEs using hot melt Surlyn 1702, followed by injection of the electrolyte. The active area at each side of these dummy cells was approximately 1 cm^2 .

2.5. Characterization

The morphologies of the prepared materials and electrodes were confirmed by field-emission scanning electron microscopy (FE-SEM; JSM-6710F, JEOL) and transmission electron microscopy (TEM; Tecnai F20 G2, FEI). The element components were investigated by X-ray photoelectron spectroscopy (XPS; PHI-5000 Versa-Probe, ULVAC-PHI) using an Al $K\alpha$ X-ray source (1486.6 eV). The Brunauer-Emmett-Teller (BET) surface area was characterized by nitrogen adsorption–desorption isotherms at 77 K

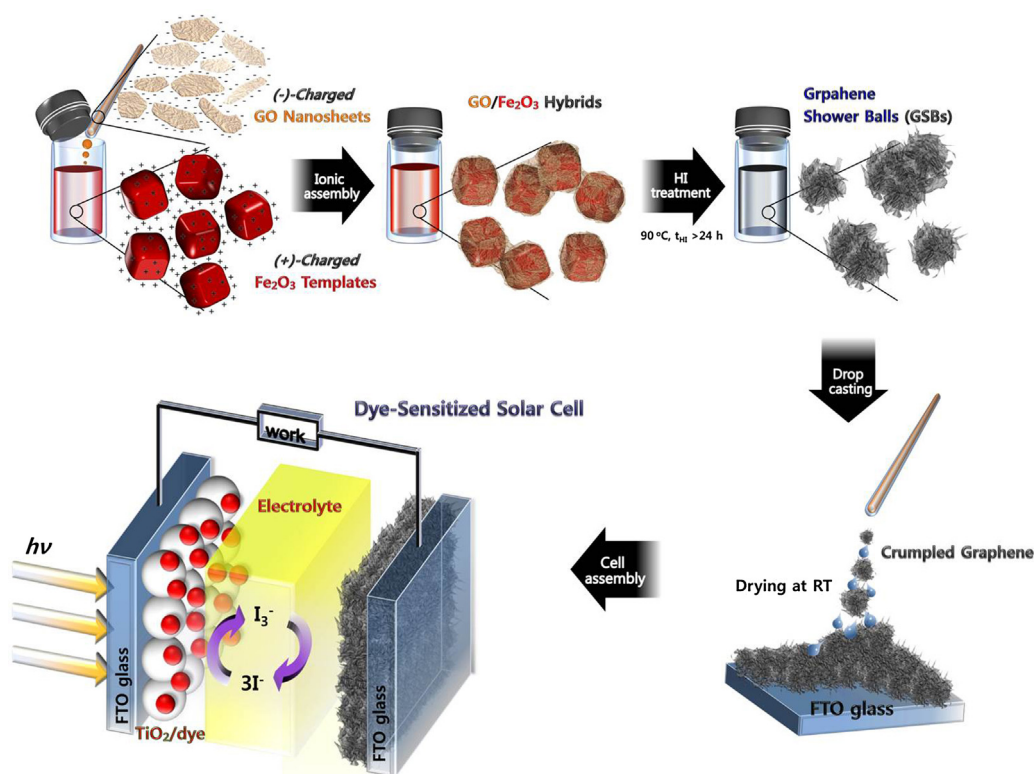


Fig. 1. Schematic illustration of the preparation of 3D interconnected macroporous graphene thin films and their application as counter electrodes in DSSCs. Negatively-charged GO nanosheets are coated on the surface of Fe_2O_3 microcubes, resulting in $\text{Fe}_2\text{O}_3/\text{GO}$ hybrids. Crumpled graphene particles are produced from the $\text{Fe}_2\text{O}_3/\text{GO}$ hybrids after a simultaneous etching–reduction process by HI treatment. The crumpled graphene films are deposited on FTO glass substrates simply by drop casting, without any binders. The fabricated crumpled graphene-based counter electrodes are applied in DSSCs with an I^-/I_3^- redox electrolyte.

(Belsorp-Max, BEL Japan Inc.). Raman spectroscopy was carried out with a Bruker RFS-100/s spectrometer using 1064 nm laser excitation, and DLS analysis was conducted using an ELS-80000 (Otsuka Electronics) instrument.

2.6. Photoelectrochemical measurements

Cyclic voltammetry (CV) was performed using a CHI440 potentiostat-galvanostat (CH Instruments Inc.) at a scan rate of 50 mV/s in an electrolyte composed of 10 mM LiI, 1 mM I_2 , and 0.1 M LiClO_4 in acetonitrile. Pt/FTO, rGO/FTO, and crumpled graphene/FTO were used as the working electrodes. A Pt wire and Ag/Ag^+ were used as the counter and reference electrodes, respectively. Standard photocurrent density–voltage (J – V) measurements were carried out using a 1600 W xenon lamp (Yamashita Denso YSS-200A solar simulator) equipped with an AM 1.5 G filter at a power of 100 mW/cm². In order to avoid overestimation caused by the additional illumination through the lateral space, each cell was covered with a black mask with an aperture [42,43]. Incident photon-to-current conversion efficiency (IPCE) spectra were obtained under short circuit conditions using a 75 W xenon lamp source and a grating monochromator (spectral resolution: 10 nm). The electrochemical impedance spectra and Tafel polarization curves were obtained for the symmetric dummy cells of each CE using a Solartron 1287 potentiostat equipped with a Solartron 1260 frequency-response detector.

3. Results and discussion

Fig. 1 shows a schematic illustration of the preparation of the 3D interconnected macroporous graphene thin films and their

application as CEs in DSSCs. The hierarchically crumpled graphene was synthesized from $\text{Fe}_2\text{O}_3/\text{GO}$ particles via a one-step chemical etching–reduction process. In this study, Fe_2O_3 particles were utilized as hard templates to design the spiky and 3D crumpled graphene structure. The Fe_2O_3 microcube templates were synthesized in bulk quantities by a sol-gel method, followed by treatment with a polyethyleneimine (PEI) suspension [40], resulting in positively charged surface characteristics ($\xi = +30$ mV) at neutral pH. The GO nanosheets prepared by a modified Hummers' method exhibited negatively charged surface characteristics ($\xi = -45$ mV) at neutral pH. Owing to the electrostatic interactions between the Fe_2O_3 microcubes and GO nanosheets, the GO nanosheets were coated on the surface of the Fe_2O_3 microcubes, resulting in $\text{Fe}_2\text{O}_3/\text{GO}$ hybrids. Subsequently, etching of the Fe_2O_3 microcubes and reduction of the GO nanosheets were simultaneously performed within the core-shell geometry by HI treatment. Crystal planes of the Fe_2O_3 microcubes with defects, such as dislocations, strains, and impurities, were preferentially etched by the HI reagent [44], resulting in spiky microstructures. At the same time, the coated GO nanosheets were chemically reduced by HI, as the iodide ions acted as catalysts. Since the coated GO nanosheets tightly and continuously adhered to the dissolving template, their structure reflected the morphology of the dissolving template during the etching–reduction process. As a result, the outer graphene layers were fully compressed into a highly crumpled structure, along with the continuously dissolving spiky template.

Since the produced crumpled graphene particles have high water dispersion stability as well as a considerably large surface area, they could be assembled into 3D macroporous films on FTO glass substrates simply by drop casting, without any binders. After drop casting, the crumpled graphene/FTO glass films were dried

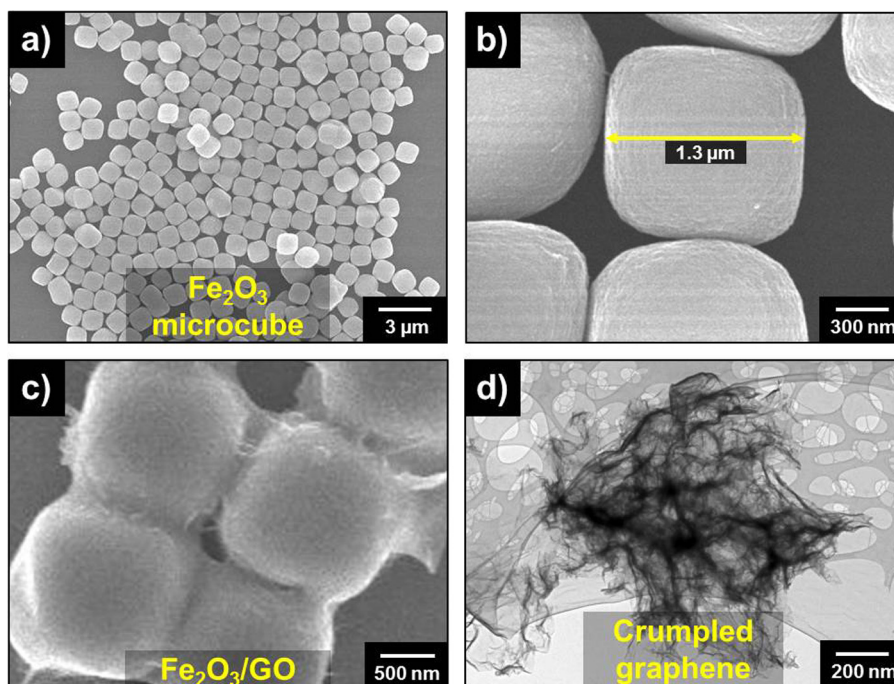


Fig. 2. SEM micrographs showing the Fe_2O_3 microcubes at (a) low and (b) high magnification. The size of hematite was estimated to be ca. $1.3\ \mu\text{m}$. Representative SEM and TEM images of (c) $\text{Fe}_2\text{O}_3/\text{GO}$ and (d) crumpled graphene. Removal of the Fe_2O_3 template and reduction of GO occurs simultaneously using HI treatment at 90°C .

at room temperature for several hours. It is noteworthy that the deposition process for the crumpled graphene films is very simple and compatible with flexible plastic substrates due to the low-temperature conditions [22,31,45,46]. The fabricated crumpled graphene CE was applied in conventional DSSCs using an N-719 dye and I^-/I_3^- redox electrolyte.

Fig. 2a and b show the synthesized pseudocubic $\alpha\text{-Fe}_2\text{O}_3$ microcube particles (JCPDS card no. 33–664, rhombohedral phase) with a uniform size of $\sim 1.3\ \mu\text{m}$ that were used as the hard template. Fig. 2c shows the $\text{Fe}_2\text{O}_3/\text{GO}$ hybrids prepared by coating the GO nanosheets onto the surface of the Fe_2O_3 microcubes using their electrostatic interactions. It was confirmed that the GO nanosheets were coated on the entire surface of the Fe_2O_3 microcubes. Fig. 2d shows the crumpled graphene produced after the simultaneous etching–reduction process, exhibiting a highly porous structure with many folds and wrinkles. This heavily crumpled 3D structure is important for application in the electrocatalytic electrode, since it can provide a large accessible surface area for electrochemical reduction, as well as superior solution processability, which is advantageous for the formation of a uniform film on the substrates. On the other hand, the rGO nanosheets are easily stacked due to the strong π – π interactions between them during drying or reduction processes, resulting in decreased surface area and solution processability [47–52].

Dynamic light scattering (DLS) was used to investigate the particle size distribution of GO and crumpled graphene in aqueous solution, as shown in Fig. 3a. The average diameter of the crumpled graphene was $1.34\ \mu\text{m}$, which had a narrow size distribution relative to GO. The inset in Fig. 3a shows the outstanding dispersibility of the crumpled graphene solution after ninety days, which means that the crumpled graphene in aqueous solution had a better sedimentation ratio than the equivalent rGO dispersion. This superb dispersion stability relates to the sedimentation velocity, which is a significant factor in particle precipitation. Stokes' law is commonly used to calculate the rate of sedimentation; it indicates that the

motion of a particle in a liquid reaches equilibrium with a uniform velocity or sedimentation rate. Stokes' law is expressed as follows:

$$V_g = d^2(\rho_p - \rho_l) / 18\eta \times G$$

where V_g is the sedimentation velocity, d is the particle diameter, ρ_p is the particle density, ρ_l is the liquid density, η is the viscosity of the liquid, and G is the gravitational acceleration. The synthesized crumpled graphene density was measured using a pycnometer. The density was calculated using the following equation:

$$\rho_p = \frac{(W_0 - P)}{(W_2 - P) - (W_1 - W_0)} \times \rho_l$$

where P is the pycnometer mass and W_0 , W_1 , and W_2 are the masses of the particles, particles and liquid, and liquid, respectively. The results showed that the density had decreased compared to that of rGO (Table 1), which was caused by the increase in volume via the simultaneous chemical etching and reduction process of $\text{Fe}_2\text{O}_3/\text{GO}$. The Stokes' equation was used to estimate the sedimentation velocities (V_g), which were 1.735×10^{-5} and 9.099×10^{-7} m/s for rGO and crumpled graphene, respectively (Table 1). The V_g of crumpled graphene was ca. 19 times slower than that of rGO. These findings demonstrated that the crumpled graphene had much better dispersibility in aqueous solution than rGO because of its highly macroporous structure.

In order to gain some insight into the structural defects, Raman analysis was conducted following etching–reduction, with increasing HI treatment time (t_{HI}). Fig. 3b shows the Raman spectra of $\text{Fe}_2\text{O}_3/\text{GO}$ ($t_{\text{HI}} = 0$ h), $\text{Fe}_2\text{O}_3/\text{graphene}$ ($t_{\text{HI}} = 1$ h), and crumpled graphene ($t_{\text{HI}} = 24$ h). It is well-known that the G peak (at around 1580 cm^{-1}) indicates a graphite carbon structure, whereas the D peak (at around 1350 cm^{-1}) indicates typical defects ascribed to structural edge effects [53,54]. The Raman spectrum of crumpled graphene as a function of etching and reduction time indicated an increased I_D/I_G intensity ratio, induced via the reduction

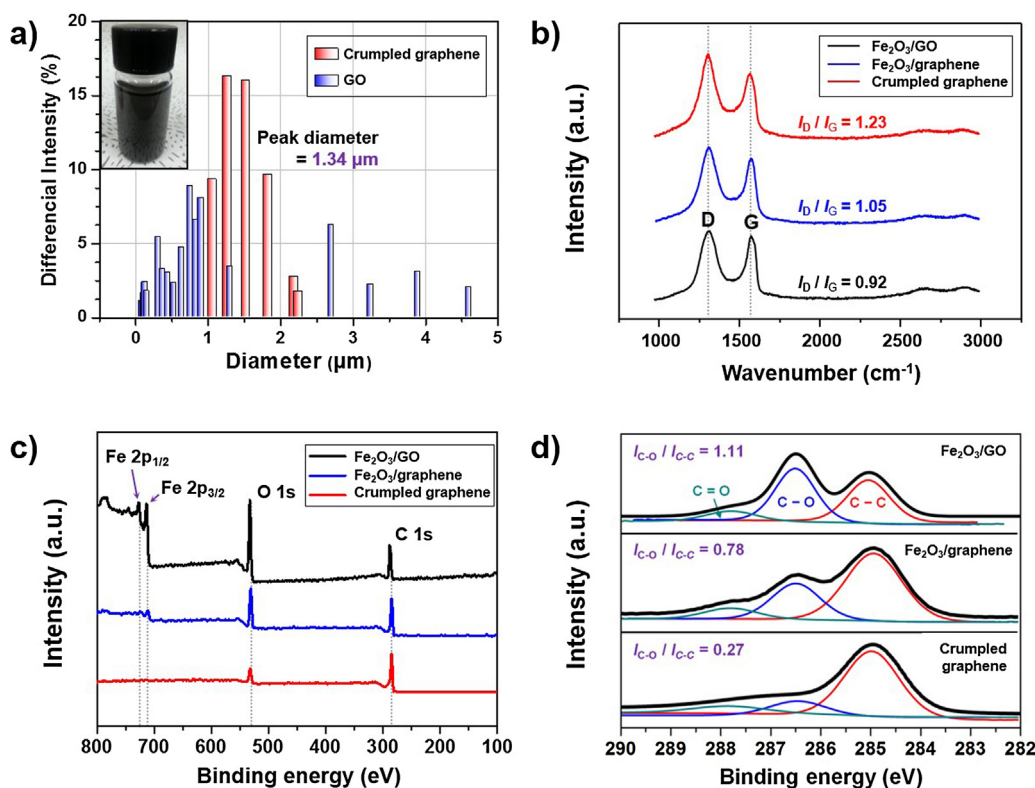


Fig. 3. (a) DLS analysis for aqueous solutions of GO and crumpled graphene. Inset: image of the crumpled graphene solution, showing good dispersibility. (b) Raman and (c and d) XPS spectra in the wide and C 1s regions of Fe₂O₃/GO ($t_{\text{HI}} = 0$ h), Fe₂O₃/graphene ($t_{\text{HI}} = 1$ h), and crumpled graphene ($t_{\text{HI}} = 24$ h) with increasing HI treatment time. The Raman spectra show G and D peaks, and the fitted lines of the XPS spectra were labeled as C–C, C–O, and C=O bonds. A weak D peak is apparent, consistent with edge effects.

Table 1

Physical parameters and sedimentation velocity of rGO and crumpled graphene in aqueous solution.

Physical parameter	rGO	Crumpled graphene
Diameter ^a (nm)	100–5000	1000–2200
Density ^b (g/cm ³)	1.85	1.12
Fluid density ^c (g/cm ³)	1	1
Fluid viscosity ^c (Pa s)	0.001	0.001
Sedimentation velocity ^d (m/s)	1.735×10^{-5}	9.099×10^{-7}

^a The average diameter was determined by TEM analyses.

^b The density was measured by pycnometry at 20 °C.

^c Distilled water was used as the dispersing medium.

^d The sedimentation velocity was calculated using the Stokes' equation.

process. This change suggested a decrease in the average size of the sp² domains upon reduction of exfoliated GO. XPS analysis was performed to investigate changes in chemical state as a result of etching–reduction (Fig. 3c and d). The initial surface of Fe₂O₃/GO mainly consisted of Fe (2p_{1/2} at 722 eV and 2p_{3/2} at 709 eV), O 1s, and C 1s, and the I_O/I_C ratio was ca. 2.22 [55]. As a result of HI treatment, the ratio gradually decreased to 0.23, and the Fe almost disappeared, which meant that the Fe₂O₃ template had been completely removed and that GO had been highly reduced. C 1s XPS analysis demonstrated that the C 1s signal for samples had three main components: C=C and C–C bond vibrations in the aromatic rings (285.0 eV), CO in the epoxy or hydroxyl groups (286.5 eV), and C=O peaks originating from carbonyl and carboxy groups (288.0 eV) [56,57]. The ratio I_{C=O}/I_{C–C} decreased from 1.1 to 0.27 via HI treatment. Judging from these data, it was evident that Fe₂O₃/GO was successfully reduced to crumpled graphene and was simultaneously involved in the chemical etching of the Fe₂O₃ template.

Fig. 4a shows the nitrogen adsorption–desorption isotherms of stacked rGO, Fe₂O₃/GO, Fe₂O₃/graphene, and crumpled graphene. As the simultaneous etching–reduction progressed, the specific

surface area and conductivity of the Fe₂O₃/GO hybrid continued to increase. The BET surface areas were 33, 71, and 459 m²/g for Fe₂O₃/GO, Fe₂O₃/graphene, and crumpled graphene, respectively. In addition, the measured conductivities were 4.7×10^{-5} , 80, and 2866 S/m for Fe₂O₃/GO, Fe₂O₃/graphene, and crumpled graphene, respectively. The nitrogen adsorption–desorption isotherms of crumpled graphene displayed a type IV isotherm with a small hysteresis loop, indicating coexisting macro and mesopores. In addition, it is obvious that the crumpled graphene has a much greater specific surface area than that of stacked rGO. The BET surface area of the stacked rGO was 19 m²/g, indicating that the surface area of crumpled graphene was approximately 24 times higher. Furthermore, as discussed above, since crumpled graphene has outstanding dispersibility in aqueous solution, it could be assembled into 3D interconnected macroporous films simply by drop casting, followed by drying at room temperature (Fig. 4b and c). The thickness of the crumpled graphene thin film deposited on FTO glass was estimated to be approximately 21 μm.

CEs based on crumpled graphene and rGO were fabricated on the FTO glasses using the same procedure. The electrocatalytic

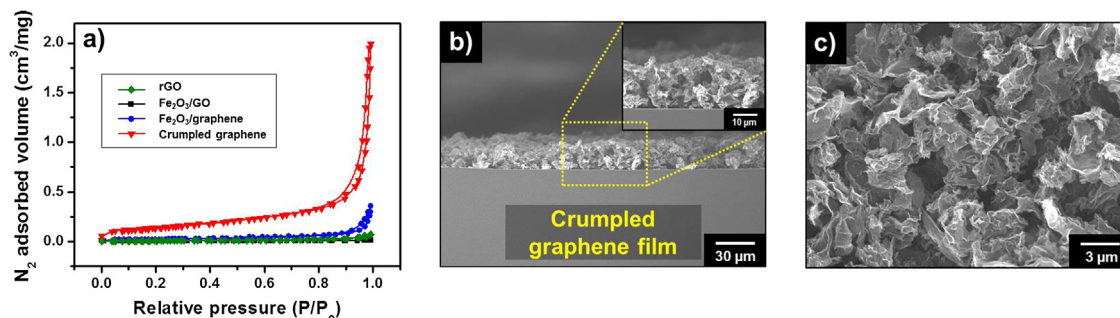


Fig. 4. (a) Nitrogen adsorption–desorption isotherms of stacked rGO, $\text{Fe}_2\text{O}_3/\text{GO}$ ($t_{\text{HI}} = 0$ h), $\text{Fe}_2\text{O}_3/\text{graphene}$ ($t_{\text{HI}} = 1$ h) and crumpled graphene ($t_{\text{HI}} = 24$ h). SEM micrographs showing the cross-section (b) and top (c) of the 3D interconnected macroporous and crumpled graphene films.

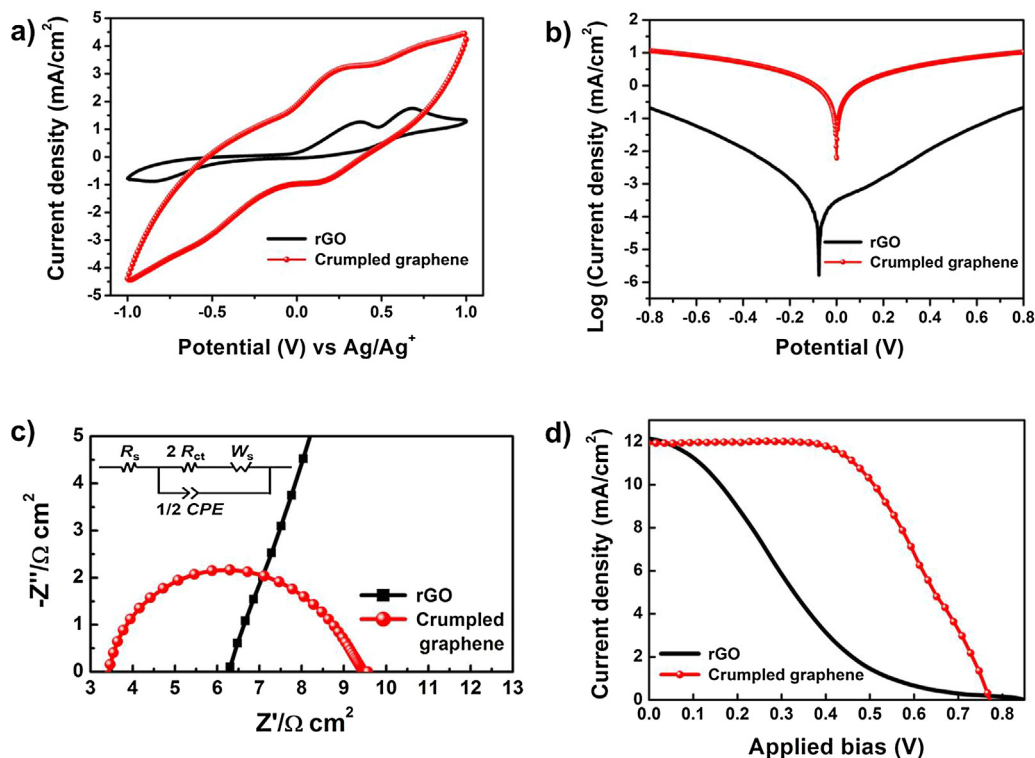


Fig. 5. (a) Cyclic voltammograms of the rGO and crumpled graphene CE for the I^-/I_3^- redox electrolyte. (b) Tafel polarization curves and (c) impedance spectra of symmetric dummy cells with each counter electrode for the I^-/I_3^- redox electrolyte. The inset of (c) shows the equivalent circuit model. (d) J – V characteristics under illumination (light intensity: $100 \text{ mW}/\text{cm}^2$, AM 1.5 G filter) of the DSSCs with each counter electrode.

activity of each CE for the I^-/I_3^- redox couple was compared by CV analysis, as shown in Fig. 5a. The pairs of redox potentials are not clear and the redox current density is considerably low for rGO, indicating an inferior electrocatalytic activity for the I^-/I_3^- redox couple. Compared to rGO, crumpled graphene exhibited a much higher redox current density, implying superior electrocatalytic activity. This is attributed to the much larger accessible surface area of crumpled graphene. The more negative and positive pairs for crumpled graphene correspond to the redox reactions of I^-/I_3^- and I_2/I_3^- , respectively [31,35,37,58].

The relative electrocatalytic activity of each CE was cross-checked by Tafel polarization measurements using symmetric dummy cells of each CE [32,34,35]. The Tafel polarization curves exhibit logarithmic current density (J) as a function of potential (V), as shown in Fig. 5b. The exchange current density (J_0) can be obtained from the intersection of the extrapolated linear anodic and cathodic branches. A steeper slope of the Tafel curve indicates a higher J_0 , and superior electrocatalytic activity. As shown in Fig. 5b, the J_0 of crumpled graphene is much higher than that of rGO, sug-

gesting that the electrocatalytic activity of crumpled graphene is far superior to that of rGO, which is consistent with the CV analysis.

For quantitative comparison of the electrocatalytic activity, impedance spectra were obtained from the same symmetric dummy cells. Nyquist diagrams of the dummy cells are shown in Fig. 5c. As shown in the inset, we utilized the equivalent circuit model comprising series resistance (R_s), impedance at the electrolyte/CE (R_{ct} and CPE), and the finite Warburg impedance (W_s) that is related to the electrolyte diffusion [37,59,60]. CPE stands for “constant phase element”, which is used instead of a capacitor in the equivalent circuit for electrodes with rough surfaces [60,61]. Double-layer capacitance (C_{dl}) can be evaluated from the CPE. After fitting the impedance spectra using ZView software, we obtained R_{ct} and C_{dl} , which are related to the electrocatalytic activity, as listed in Table 2. The R_{ct} of crumpled graphene was 4 orders of magnitude lower than that of rGO, indicating significantly superior electrocatalytic activity. In addition, crumpled graphene showed a higher C_{dl} compared to that of rGO, due to a large surface area for electrochemical reaction. The results of CV, Tafel

Table 2
Summary of J - V characteristics for rGO, and crumpled graphene CEs, and parameters determined by fitting the impedance spectra of symmetric dummy cells with each CE.

Electrode	J_{sc} (mA/cm ²)	V_{oc} (V)	Fill factor (%)	Efficiency (%)	R_{ct} (Ω cm ²)	C_{dl} (μ F/cm ²)
rGO	12.15	0.851	18	1.86	1.42×10^4	28.70
Crumpled graphene	11.93	0.771	56	5.15	2.86	51.16

polarization measurements, and impedance analysis show good agreement, indicating that the electrocatalytic activity of crumpled graphene is greatly superior to that of rGO.

Finally, the prepared CEs were introduced into DSSCs containing an I^-/I_3^- redox electrolyte. Fig. 5d shows the J - V characteristics of the DSSCs with each CE, and the photovoltaic performance parameters are summarized in Table 2. The conversion efficiency (η) of crumpled graphene ($\eta = 5.15\%$) was significantly higher (2.8 times higher) than that of rGO ($\eta = 1.86\%$). The short-circuit current density (J_{sc}) was not greatly different among the CEs, and the J_{sc} trend agrees well with the IPCE data (Fig. S1 in the Supporting Information). The dominant factor in determining η was the fill factor (FF), which is closely related to the electrocatalytic activity of the CE [31,33–35]. The FF of crumpled graphene was 3.1 times higher compared to rGO. The superior electrocatalytic activity of crumpled graphene resulting from the greatly larger surface area for electrochemical reaction leads to the much higher η compared to rGO.

At the same condition, the conventional Pt CE prepared by thermal decomposition at a high temperature (400 °C) showed a conversion efficiency of 7.19% (Fig. S2 in the Supporting Information). Although the photovoltaic performance of Pt CE is superior than that of the crumpled graphene CE, it is noteworthy that the crumpled graphene CE exhibited a reasonable efficiency without any dopants or high-temperature annealing in this study. This means that the fundamental electrocatalytic activity resulting from the large number of electrochemical reaction sites is sufficiently effective for the reduction of the I^-/I_3^- redox couple. Furthermore, the deposition of crumpled graphene on the substrate (FTO glass) and drying were performed at room temperature, meaning the method could be applied to flexible plastic substrates. Therefore, the crumpled graphene CE proposed in this study is a promising material for the fabrication of low-cost and flexible DSSCs, as it can be fabricated via a facile and simple process. Further work is under way to develop more efficient CEs that surpass the electrocatalytic activity of Pt by a modification of chemical composition of the crumpled graphene.

4. Conclusions

In this study, we developed a simple and facile process to fabricate efficient and low-cost CEs of DSSCs based on highly crumpled graphene. 3D crumpled graphene containing many folds and wrinkles was synthesized by a one-step chemical etching and reduction process, using Fe_2O_3 microcubes as hard templates. Owing to the superior solution processability of the synthesized crumpled graphene, it could be assembled into uniform films on FTO glass substrates, simply by drop casting, without the addition of binders. Furthermore, the crumpled graphene CE exhibited greatly enhanced electrocatalytic activity for the I^-/I_3^- redox couple, compared to that of the conventional rGO, even without dopants or a high-temperature annealing process. This was mainly attributed to its significantly larger accessible surface area for electrochemical reduction. As a result, DSSCs containing the crumpled graphene CE showed greatly enhanced FF and conversion efficiency compared to rGO. The results offer valuable insight into the development of

highly efficient, low-cost and flexible CEs of next-generation photoelectrochemical solar cells based on graphene materials.

Acknowledgements

This work was supported from the Technology Development Program to Solve Climate Changes (2015M1A2A2056824), the Global Frontier R&D Program on Center for Multiscale Energy System (2012M3A6A7054856), and 2015 University-Institute cooperation program funded by the National Research Foundation under the Ministry of Science, ICT & Future Planning, Korea; this work was also supported by the KU-KIST Graduate School and KIST institutional programs.

Appendix A. Supplementary data

Supplementary data associated with this article can be found, in the online version, at <http://dx.doi.org/10.1016/j.apcatb.2016.04.008>.

References

- [1] A.K. Geim, K.S. Novoselov, *Nat. Mater.* 6 (2007) 183.
- [2] Z.-S. Wu, G. Zhou, L.-C. Yin, W. Ren, F. Li, H.-M. Cheng, *Nano Energy* 1 (2012) 107.
- [3] Y. Chen, J. Zhu, B. Qu, B. Lu, Z. Xu, *Nano Energy* 3 (2014) 88.
- [4] H. Qian, Y. Ma, Q. Yang, B. Chen, Y. Liu, X. Guo, S. Lin, J. Ruan, X. Liu, L. Tong, Z.L. Wang, *ACS Nano* 8 (2014) 2584.
- [5] Y. Xue, Y. Ding, J. Niu, Z. Xia, A. Roy, H. Chen, J. Qu, Z.L. Wang, L. Dai, *Sci. Adv.* 1 (2015) 1400198.
- [6] X. Wang, L. Zhi, K. Müllen, *Nano Lett.* 8 (2008) 323.
- [7] J.Y. Lee, K.-H. Lee, Y.J. Kim, J.S. Ha, S.-S. Lee, J.G. Son, *Adv. Funct. Mater.* 25 (2015) 3606.
- [8] S.-H. Yu, D.E. Conte, S. Baek, D.-C. Lee, S.-K. Park, K.J. Lee, Y. Piao, Y.-E. Sung, N. Pinna, *Adv. Funct. Mater.* 23 (2013) 4293.
- [9] L. Kavan, J.-H. Yum, M.K. Nazeeruddin, M. Grätzel, *ACS Nano* 5 (2011) 9171.
- [10] M.J. Ju, I.-Y. Jeon, J.C. Kim, K. Lim, H.-J. Choi, S.-M. Jung, I.T. Choi, Y.K. Eom, Y.J. Kwon, J. Ko, J.-J. Lee, H.K. Kim, J.-B. Baek, *Adv. Mater.* 26 (2014) 3055.
- [11] M.J. Ju, I.-Y. Jeon, K. Lim, J.C. Kim, H.-J. Choi, I.T. Choi, Y.K. Eom, Y.J. Kwon, J. Ko, J.-J. Lee, J.-B. Baek, H.K. Kim, *Energy Environ. Sci.* 7 (2014) 1044.
- [12] H. Choi, H. Kim, S. Hwang, Y. Han, M. Jeon, *J. Mater. Chem.* 21 (2011) 7548.
- [13] X. Xu, D. Huang, K. Cao, M. Wang, S.M. Zakeeruddin, M. Grätzel, *Sci. Rep.* 3 (2013) 1489.
- [14] H.-J. Ahn, I.-H. Kim, J.-C. Yoon, S.-I. Kim, J.H. Jang, *Chem. Commun.* 50 (2014) 2412.
- [15] Q. Luo, F. Hao, S. Wang, H. Shen, L. Zhao, J. Li, M. Grätzel, H. Lin, *J. Phys. Chem. C* 118 (2014) 17010.
- [16] Z. Wang, P. Li, Y. Chen, J. He, J. Liu, W. Zhang, Y. Li, *J. Power Sour.* 263 (2014) 246.
- [17] M. Al-Mamun, J.-Y. Kim, Y.-E. Sung, J.-J. Lee, S.-R. Kim, *Chem. Phys. Lett.* 561 (2013) 115.
- [18] I.V. Lightcap, P.V. Kamat, *J. Am. Chem. Soc.* 134 (2012) 7109.
- [19] B. O' Regan, M. Grätzel, *Nature* 353 (1991) 737.
- [20] S. Ito, S.M. Zakeeruddin, P. Comte, P. Liska, D. Kuang, M. Grätzel, *Nat. Photon.* 2 (2008) 693.
- [21] K. Lee, S. Park, M.J. Ko, K. Kim, N.-G. Park, *Nat. Mater.* 8 (2009) 665.
- [22] A. Hagfeldt, G. Boschloo, L. Sun, L. Kloo, H. Pettersson, *Chem. Rev.* 110 (2010) 6595.
- [23] J.-H. Yum, S.-J. Moon, C.S. Karthikeyan, H. Wietasch, M. Thelakkat, S.M. Zakeeruddin, M.K. Nazeeruddin, M. Grätzel, *Nano Energy* 1 (2012) 6.
- [24] J. Bae, Y.J. Park, M. Lee, S.N. Cha, Y.J. Choi, C.S. Lee, J.M. Kim, Z.L. Wang, *Adv. Mater.* 23 (2011) 3446.
- [25] S.H. Kang, S.-H. Choi, M.-S. Kang, J.-Y. Kim, H.-S. Kim, T. Hyeon, Y.-E. Sung, *Adv. Mater.* 20 (2008) 54.
- [26] S.J. Park, K. Yoo, J.-Y. Kim, J.Y. Kim, D.-K. Lee, B. Kim, H. Kim, J.H. Kim, J. Cho, M.J. Ko, *ACS Nano* 7 (2013) 4050.

- [27] J.-Y. Kim, J.S. Kang, J. Shin, J. Kim, S.-J. Han, J. Park, Y.-S. Min, M.J. Ko, Y.-E. Sung, *Nanoscale* 7 (2015) 8368.
- [28] M.-W. Lee, J.-Y. Kim, H.J. Son, J.Y. Kim, B. Kim, H. Kim, D.-K. Lee, K. Kim, D.-H. Lee, M.J. Ko, *Sci. Rep.* 5 (2015) 7711.
- [29] J.-Y. Kim, K.-H. Lee, J. Shin, S.H. Park, J.S. Kang, K.S. Han, M.M. Sung, N. Pinna, Y.-E. Sung, *Nanotechnology* 25 (2014) 504003.
- [30] J.-Y. Kim, S.H. Kang, H.S. Kim, Y.-E. Sung, *Langmuir* 26 (2010) 2864.
- [31] K. Yoo, J.-Y. Kim, J.A. Lee, J.S. Kim, D.-K. Lee, K. Kim, J.Y. Kim, B. Kim, H. Kim, W.M. Kim, J.H. Kim, M.J. Ko, *ACS Nano* 9 (2015) 3760.
- [32] J.S. Kang, M.-A. Park, J.-Y. Kim, S.H. Park, D.Y. Chung, S.-H. Yu, J. Kim, J. Park, J.-W. Choi, K.J. Lee, J. Jeong, M.J. Ko, K.-S. Ahn, Y.-E. Sung, *Sci. Rep.* 5 (2015) 10450.
- [33] I. Jeong, J. Lee, K.L.V. Joseph, H.I. Lee, J.K. Kim, S. Yoon, J. Lee, *Nano Energy* 9 (2014) 392.
- [34] I. Jeong, C. Jo, A. Anthonysamy, J.-M. Kim, E. Kang, J. Hwang, E. Ramasamy, S.-W. Rhee, J.K. Kim, K.-S. Ha, K.-W. Jun, J. Lee, *ChemSusChem* 6 (2013) 299.
- [35] M. Wu, X. Lin, Y. Wang, L. Wang, W. Guo, D. Qi, X. Peng, A. Hagfeldt, M. Grätzel, T. Ma, *J. Am. Chem. Soc.* 134 (2012) 3419.
- [36] D. Yu, E. Nagelli, F. Du, L. Dai, *J. Phys. Chem. Lett.* 1 (2010) 2165.
- [37] J.D. Roy-Mayhew, D.J. Bozym, C. Punckt, I.A. Aksay, *ACS Nano* 4 (2010) 6203.
- [38] T. Sugimoto, K. Sakata, *J. Colloid Interface Sci.* 152 (1992) 587.
- [39] W.S. Hummers, R.E. Offeman, *J. Am. Chem. Soc.* 80 (1958) 1339.
- [40] S. Chibowski, J. Patkowski, E. Gradka, *J. Colloid Interface Sci.* 329 (2009) 1.
- [41] H.-J. Koo, J. Park, B. Yoo, K. Yoo, K. Kim, N.-G. Park, *Inorg. Chim. Acta* 361 (2008) 677.
- [42] S. Ito, K. Nazeeruddin, P. Liska, P. Comte, R. Charvet, P. Peichy, M. Jirousek, A. Kay, S.M. Zakeeruddin, M. Grätzel, *Prog. Photovolt.: Res. Appl.* 14 (2006) 589.
- [43] J. Park, H.-J. Koo, B. Yoo, K. Yoo, K. Kim, W. Choi, N.-G. Park, *Sol. Energy Mater. Sol. Cells* 91 (2007) 1749.
- [44] R.M. Cornell, U. Schwertmann, *The Iron Oxides: Structure, Properties, Reactions, Occurrences and Uses*, 2nd ed., John Wiley & Sons Weinheim, Germany, 2006.
- [45] Y. Li, D.-K. Lee, J.Y. Kim, B. Kim, N.-G. Park, K. Kim, J.-H. Shin, I.-S. Choi, M.J. Ko, *Energy Environ. Sci.* 5 (2012) 8950.
- [46] Y. Li, K. Yoo, D.-K. Lee, J.Y. Kim, H. Kim, B. Kim, M.J. Ko, *Nanoscale* 5 (2013) 4711.
- [47] S. Park, R.S. Ruoff, *Nat. Nanotech.* 4 (2009) 217.
- [48] W. Gao, L.B. Alemany, L. Ci, P.M. Ajayan, *Nat. Chem.* 1 (2009) 403.
- [49] D.R. Dreyer, S. Park, C.W. Bielawski, R.S. Ruoff, *Chem. Soc. Rev.* 39 (2010) 228.
- [50] D. Li, M.B. Muller, S. Gilje, R.B. Kaner, G.G. Wallace, *Nat. Nanotech.* 3 (2008) 101.
- [51] Y.J. Dappe, M.A. Basanta, F. Flores, J. Ortega, *Phys. Rev. B* 74 (2006) 205434.
- [52] J.Y. Luo, H.D. Jang, T. Sun, L. Xiao, Z. He, A.P. Katsoulidis, M.G. Kanatzidis, J.M. Gibson, J. Huang, *ACS Nano* 5 (2011) 8943.
- [53] A. Ferrari, J. Meyer, V. Scardaci, C. Casiraghi, M. Lazzeri, F. Mauri, S. Piscanec, D. Jiang, K. Novoselov, S. Roth, A.K. Geim, *Phys. Rev. Lett.* 97 (2006) 187401.
- [54] K.-Y. Shin, J.-Y. Hong, J. Jang, *Adv. Mater.* 23 (2011) 2113.
- [55] R. Barik, S.K. Tripathy, M. Mohapatra, *J. Mater. Sci.* 49 (2014) 5345.
- [56] S. Park, R.S. Ruoff, *Nat. Nanotech.* 4 (2009) 217.
- [57] S. Pei, H.M. Cheng, *Carbon* 50 (2012) 3210.
- [58] S.H. Park, K.-H. Shin, J.-Y. Kim, S.J. Yoo, K.J. Lee, J. Shin, J.W. Choi, J. Jang, Y.-E. Sung, *J. Photochem. Photobiol. A: Chem.* 245 (2012) 1.
- [59] J.-Y. Kim, K.J. Lee, S.H. Kang, J. Shin, Y.-E. Sung, *J. Phys. Chem. C* 115 (2011) 19979.
- [60] J.-Y. Kim, J.Y. Kim, D.-K. Lee, B. Kim, H. Kim, M.J. Ko, *J. Phys. Chem. C* 116 (2012) 22759.
- [61] C. Longo, A.F. Nogueira, M.A. De Paoli, H. Cachet, *J. Phys. Chem. B* 106 (2002) 5925.